Selective Periodic Disturbance Elimination Using Extended Harmonic State Observer for Smooth Speed Control in PMSM Drives

Mingjin Hu, *Student Member, IEEE*, Wei Hua, *Senior Member, IEEE*, Zuo Wang, *Member, IEEE*, Shihua Li, *Fellow, IEEE*, Peixin Wang, *Student Member, IEEE*, and Yuchen Wang

***Abstract*—The elimination of periodic torque disturbance in permanent magnet synchronous machine (PMSM) drives is a multi-frequency control task, and adding resonant parts to the controller has an impact on the robustness of the system. This article aims to address the torque-ripple reduction in PMSM drives for smooth speed control, where an extended harmonic state observer (EHSO) is designed for estimation and attenuation of the selective periodic disturbance. The defects of applying the conventional bandwidth-parameterization method to the harmonic disturbance observer are explored. To improve the disturbance-rejection capability and the relative stability, a pole-placement strategy is proposed and analyzed through sensitivity function, which can preserve the comparable dynamic performance as the conventional extended state observer at the low-frequency range. The proposed EHSO also features easy parameter tuning and a modular structure for multiple harmonic disturbance rejection. Finally, the proposed method is evaluated on a laboratory PMSM platform.**

***Index Terms*—Extended harmonic state observer (EHSO), permanent magnet synchronous machine (PMSM) drives, resonant control, torque ripple.**

I. Introduction

TORQUE ripple always causes undesirable speed fluctuation, vibration, and acoustic noise to the permanent magnet synchronous machine (PMSM) drives, and consequently degrades the control performance. The dominant torque ripple sources can be summarized as follows.

1) *Cogging torque*: The cogging torque is a periodic function of the rotor position. Generally, the orders of its components are several times of the lowest common multiple of stator slots and rotor pole-pairs of a PMSM [1]. In addition, the manufacturing tolerances will arise extra cogging torque components with other orders [2].
2) *Flux harmonics:* The nonsinusoidal flux density distribution in the air gap results in flux harmonics, which interact with the stator currents and lead to torque ripples.
3) *Current harmonics:* Current harmonics majorly result from the flux harmonics and inverter nonlinearity, which will also interact with the PM flux and generate torque harmonics.
4) *Current measurement error:* The offset error and scaling error in the current measurement result are the first- and second-order harmonic torque (of the fundamental frequency) [3].

From a system perspective, the reduction of torque ripple requires good coordination among machine design, manufacture, sensors, converter, and control. Many research studies on machine design have been carried out to interpret and optimize torque ripples [1], [4]. However, reducing torque ripples sometimes is not the primary goal in the design stage as it may be costly and lead to degradation in power or torque [5]. In contrast, control techniques to minimize torque fluctuation are preferable for flexibility and low cost.

The torque ripples caused by armature-current distortion can be reduced by compensating for inverter nonlinearity [6], calibration of current sensor [7], and directly suppressing the harmonic currents [8]. As for other types of torque ripples, such as the cogging torque, their effect can be counteracted by harmonic-current injection, which can be further divided into the feedforward and feedback control strategies. The feedforward strategies utilize the prior knowledge from the machine model [9] or experimental identifications [10] to determine the optimal current reference for torque ripple compensation. However, accurate machine information may not be available and such dependence will lead to poor robustness.

The feedback control strategies acquire the injected currents in a closed-loop way using the measured currents, speed, and position [11]–[17]. Since the torque ripples behave as periodic disturbance to the speed loop, and generate harmonic components in rotor speed with the same frequencies, minimizing torque harmonics is equivalent to reducing the corresponding harmonic speed components. The iterative learning control [13]

Manuscript received 1 March 2022; revised 30 April 2022; accepted 22 June 2022. Date of publication 29 June 2022; date of current version 26 July 2022. This work was supported in part by the Key R&D Program under Grant 2021YFB2500701, in part by the National Natural Science Foundation of China under Grant 51825701, and in part by the Scientific Research Foundation of Graduate School of Southeast University under Grant YBYP2148. Recommended for publication by Associate Editor J. Zhang. *(Corresponding author: Wei Hua.)*

Mingjin Hu, Wei Hua, Peixin Wang, and Yuchen Wang are with the School of Electrical Engineering, Southeast University, Nanjing 210096, China (e-mail: hmj@seu.edu.cn; huawei1978@seu.edu.cn; wangpeixin@seu.edu.cn; wangyuchen1994@seu.edu.cn).

Zuo Wang and Shihua Li are with the Key Laboratory of Measurement and Control of CSE, Ministry of Education, School of Automation, Southeast University, Nanjing 210096, China (e-mail: z.wang@seu.edu.cn; lsh@seu.edu.cn).

Color versions of one or more figures in this article are available at https://doi.org/10.1109/TPEL.2022.3187125.

Digital Object Identifier 10.1109/TPEL.2022.3187125

and repetitive control [14]–[16] are suitable in this scenario. As the frequencies of torque ripples vary accordingly with the rotor speed, it would be challenging to implement repetitive control in variable-speed PMSM drives. In the literature [17], Xia *et al.* use the proportional-integral-resonant (PIR) controller to realize smooth speed control. To avoid exciting the resonant mode in transient states, Xia *et al.* [17] suggest temporarily turning OFF the resonant controller when the speed error exceeds a certain threshold.

In addition, the disturbance-observer-based methods are other candidates for attenuating the effect of harmonic disturbance [18]–[23]. In [24], the disturbance observer (DOB) is utilized to compensate for the low-frequency torque ripples. The extended state observer (ESO) can offer attenuation for harmonic disturbance within its bandwidth, and the high-order ESO would achieve further improvement [18]. As for harmonic disturbance with higher frequency, Guo *et al.* [19] add parallel generalized integrators to the ESO for harmonic state observation, however, its performance analysis and parameter tuning become more complicated. In [20], the resonant parts as the internal model of harmonic torque are augmented to the DOB for accurate estimation, by which two dominant torque harmonics are estimated and attenuated.

When multifrequency components are to be estimated, the design and tuning of the disturbance estimator become more critical. The bandwidth-parameterization method [25] suggests assigning the observer poles of ESO to multiple ones for tuning simplicity and efficiency, which is adopted in [21] for suppression of multiple harmonics in PMSM drives. The design criteria in [20] advocate that the dominant observer pole for speed estimation should be much faster than the poles for harmonic states, whereas the latter should be much faster than the harmonic frequencies. A similar strategy is also employed in [22] for grid-tied converters. However, in the literature [26], Pérez-Estévez *et al.* reveal that the multifrequency DOB with such frequency-domain characteristics will lead to a poor stability margin. Instead, Pérez-Estévez *et al.* [26] utilize the linear-quadratic-regulator (LQR) design for the DOB to improve the robustness, which minimizes the estimation error in the time domain. Nevertheless, this method may not be suitable for variable-speed PMSM drives because of the varying harmonic frequencies, which need to solve the Riccati equation online and causes a significant computational burden for current microcontrollers.

This article designs an extended harmonic state observer (EHSO) for attenuation of selective periodic torque disturbance in PMSM drives. To address the stability issues when the constant disturbance and multiple harmonic disturbance are to be observed, a pole-placement strategy is proposed for improved robustness and disturbance-rejection capability. The developed EHSO features simple parameter tuning and a modular architecture, and thus is suitable for implementation in variable-speed drives. The rest of this article is organized as follows. Section II introduces the system model. In Section III, the EHSO is developed for harmonic disturbance estimation and attenuation. Experimental verification is given in Section V. Finally, Section VI concludes this article.

II. System Model

A. Mechanical Model of PMSM Drives

The mechanical dynamic of a single-mass surface-mounted PMSM drive is given by

$$\begin{aligned}\frac{\mathrm{d}}{\mathrm{d}t}\,\omega_m &= \frac{1.5P_r\psi_m}{J}\,i_q - \frac{1}{J}\left(T_L + T_h + B_m\omega_m\right)\\ &= a\omega_m + b\left(i_q + d_{ex}\right)\end{aligned} \tag{1}$$

where J is the total moment of inertia, B_m is the friction constant, ω_m is the angular rotor speed, P_r is rotor pole-pairs, ψ_m is the PM flux linkage, i_q is the *q*-axis current, $a = -B_m/J$, $b = 1.5P_r\psi_m/J$, T_L is the load torque, T_h represents all the periodic torque introduced in Section I, and $d_{ex} = -(T_L + T_h)/(1.5P_r\psi_m)$ is the external disturbance in the input channel.

Equation (1) is further rewritten as a nominal model

$$\frac{\mathrm{d}}{\mathrm{d}t}\,\omega_m = a_0\,\omega_m + b_0\left(i_q + d\right) \tag{2}$$

where a_0 and b_0 are the nominal value of a and b, respectively, and $d = (b_0^{-1}b - 1)\,i_q + b_0^{-1}bd_{ex} + b_0^{-1}(a - a_0)\omega_m$ is the lumped disturbance that includes the effect of both the external disturbance and model uncertainty.

B. Model of Disturbance

An h-order harmonic disturbance $w_h(t)$ in the time domain can be defined using its frequency $\omega_h = h\omega_m$, magnitude M_h, and initial phase ϕ_h as

$$w_h\,(t) = M_h\,\cos\left(\omega_h t + \phi_h\right). \tag{3}$$

In this article, the lumped disturbance d is supposed to be the sum of several harmonic components and a constant component w_0 that represents the slow-varying disturbance, which is modeled by

$$d = w_0 + \sum_{i\,=\,1}^{n} w_{h_i}. \tag{4}$$

Noting that the dynamics of $w_h(t)$ can be formulated by

$$\frac{\mathrm{d}}{\mathrm{d}t}\begin{bmatrix} w_h \\ \zeta_h \end{bmatrix} = \underbrace{\begin{bmatrix} 0 & 1 \\ -\omega_h^2 & 0 \end{bmatrix}}_{\boldsymbol{\Omega}_h}\begin{bmatrix} w_h \\ \zeta_h \end{bmatrix} \tag{5}$$

where $\zeta_h = \mathrm{d}w_h/\mathrm{d}t$ is an auxiliary state.

Consequently, the multifrequency disturbance in (4) is rewritten in state-space form as

$$\frac{\mathrm{d}}{\mathrm{d}t}\underbrace{\begin{bmatrix} w_0 \\ w_{h_1} \\ \zeta_{h_1} \\ \vdots \\ w_{h_n} \\ \zeta_{h_n} \end{bmatrix}}_{\boldsymbol{w}} = \underbrace{\begin{bmatrix} \mathbf{0} & \mathbf{0} & \mathbf{0} & \dots & \mathbf{0} \\ \mathbf{0} & \boldsymbol{\Omega}_{h_1} & \mathbf{0} & \dots & \mathbf{0} \\ \mathbf{0} & \mathbf{0} & \boldsymbol{\Omega}_{h_2} & \dots & \mathbf{0} \\ \vdots & \vdots & \vdots & \ddots & \mathbf{0} \\ \mathbf{0} & \mathbf{0} & \mathbf{0} & \mathbf{0} & \boldsymbol{\Omega}_{h_n} \end{bmatrix}}_{\boldsymbol{A}_d}\begin{bmatrix} w_0 \\ w_{h_1} \\ \zeta_{h_1} \\ \vdots \\ w_{h_n} \\ \zeta_{h_n} \end{bmatrix} \tag{6}$$

$$d = \underbrace{[11, 0, \dots, 10]}_{\boldsymbol{C}_d}\,\boldsymbol{w} \tag{7}$$

where $\boldsymbol{w}$ is the extended state vector of the lumped disturbance. Obviously, 0 and $\pm j\omega_{h_i}$ are the eigenvalues of $\boldsymbol{A}_d$.

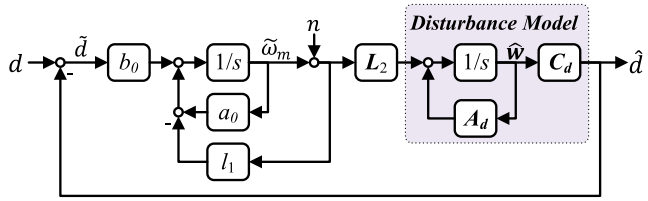

Fig. 1. Equivalent model for the disturbance estimation.

III. Design of EHSO

In this section, the EHSO is to be developed for accurate and fast estimation of the torque disturbance, including the constant load torque and harmonic torque. By augmenting the nominal model (2) with the disturbance model (6), the EHSO is formulated as

$$\begin{cases} \frac{\mathrm{d}}{\mathrm{d}t}\underbrace{\begin{bmatrix}\hat{\omega}_m\\ \hat{\boldsymbol{w}}\end{bmatrix}}_{\hat{\boldsymbol{x}}_1} = \underbrace{\begin{bmatrix}a_0 & b_0\boldsymbol{C}_d\\ \boldsymbol{0} & \boldsymbol{A}_d\end{bmatrix}}_{\boldsymbol{A}_1}\underbrace{\begin{bmatrix}\hat{\omega}_m\\ \hat{\boldsymbol{w}}\end{bmatrix}}_{\hat{\boldsymbol{x}}_1} + \underbrace{\begin{bmatrix}b_0\\ \boldsymbol{0}\end{bmatrix}}_{\boldsymbol{B}_1} i_q + \underbrace{\begin{bmatrix}l_1\\ \boldsymbol{L}_2\end{bmatrix}}_{\boldsymbol{L}}(y-\hat{y}) \\ \hat{y} = \underbrace{\begin{bmatrix}1 & \boldsymbol{0}\end{bmatrix}}_{\boldsymbol{C}_1}\hat{\boldsymbol{x}}_1, \hat{d} = \underbrace{\begin{bmatrix}0 & \boldsymbol{C_d}\end{bmatrix}}_{\boldsymbol{C}_{1\boldsymbol{d}}}\hat{\boldsymbol{x}}_1 \end{cases} \tag{8}$$

where $y = \omega_m + n$, n is the measurement noise, $\hat{\omega}_m$ and $\hat{\boldsymbol{w}} = [\hat{w}_0, \hat{w}_{h_1}, \hat{\zeta}_{h_1}, \ldots, \hat{w}_{h_n}, \hat{\zeta}_{h_n}]^T$ are the estimations for ω_m and $\boldsymbol{w}$, respectively, and $\boldsymbol{L} = [l_1\ \boldsymbol{L}_2^T]^T$ is the observer gain.

The observer (8) is stable if all roots of the characteristic polynomial

$$\Phi(s) = \det(s\boldsymbol{I} - \boldsymbol{A}_1 + \boldsymbol{L}\boldsymbol{C}_1) \tag{9}$$

are in the left plane. The actual q-axis current i_q is fed to the observer instead of the current reference i_q^*, thus the consistency between the observer and the real plant states is maintained, and the wind-up problem can be avoided [27].

Rewriting (8) in terms of the state error $\tilde{\omega}_m = \hat{\omega}_m - \omega_m$ as

$$\frac{\mathrm{d}}{\mathrm{d}t}\begin{bmatrix}\tilde{\omega}_m\\ \hat{\boldsymbol{w}}\end{bmatrix} = \underbrace{\begin{bmatrix}a_0 - l_1 & b_0\boldsymbol{C}_d\\ -\boldsymbol{L}_2 & \boldsymbol{A}_d\end{bmatrix}}_{\boldsymbol{A}_1 - \boldsymbol{L}\boldsymbol{C}_1}\begin{bmatrix}\tilde{\omega}_m\\ \hat{\boldsymbol{w}}\end{bmatrix} - \underbrace{\begin{bmatrix}b_0\\ \boldsymbol{0}\end{bmatrix}}_{\boldsymbol{B}_1} d + \underbrace{\begin{bmatrix}l_1\\ \boldsymbol{L}_2\end{bmatrix}}_{\boldsymbol{L}} n. \tag{10}$$

Based on (10), the block diagram of the equivalent model for the disturbance estimation is derived, as shown in Fig. 1, where the disturbance model is embedded. The disturbance estimation error is given by $\tilde{d} = d - \hat{d} = -\boldsymbol{C}_{1\boldsymbol{d}}\hat{\boldsymbol{x}}_1 + d$, thus the sensitivity function of the disturbance estimation loop, $S_d(s) \overset{\text{def}}{=} \tilde{d}(s)/d(s)$, is calculated by the characteristic equation and zeros polynomial [28, Eq. (7.64)], and simplified as

$$\begin{aligned} S_d(s) &= \frac{\det\left(\begin{bmatrix}s\boldsymbol{I} - \boldsymbol{A}_1 + \boldsymbol{L}\boldsymbol{C}_1 & \boldsymbol{B}_1\\ -\boldsymbol{C}_{1d} & 1\end{bmatrix}\right)}{\det(s\boldsymbol{I} - \boldsymbol{A}_1 + \boldsymbol{L}\boldsymbol{C}_1)} \\ &= \frac{\det(s\boldsymbol{I} - \boldsymbol{A}_1 + \boldsymbol{L}\boldsymbol{C}_1 + \boldsymbol{B}_1\boldsymbol{C}_{1d})}{\det(s\boldsymbol{I} - \boldsymbol{A}_1 + \boldsymbol{L}\boldsymbol{C}_1)} \\ &= \frac{(s - a_0 + l_1)\cdot\det(s\boldsymbol{I} - \boldsymbol{A}_d)}{\det(s\boldsymbol{I} - \boldsymbol{A}_1 + \boldsymbol{L}\boldsymbol{C}_1)}. \end{aligned} \tag{11}$$

We also define $T_d(s) = \hat{d}(s)/d(s) = 1 - S_d(s)$ as the response from $d(s)$ to $\hat{d}(s)$. Equation (11) gives a general expression for the disturbance estimation regardless of $\boldsymbol{A}_d$. It is shown that the eigenvalues of $\boldsymbol{A}_1 - \boldsymbol{L}\boldsymbol{C}_1$ determine the poles of $S_d(s)$, whereas the eigenvalues of $\boldsymbol{A}_d$ are the zeros, indicating that the estimation error arising from the lumped disturbance will be removed at the frequencies defined by $\det(j\omega\boldsymbol{I} - \boldsymbol{A}_d) = 0$ in steady state.

In the following sections, the conventional ESO with $\boldsymbol{A}_d = 0$ for constant disturbance will be briefly studied as a baseline, and then the EHSO will be developed for additional harmonic estimation.

A. Conventional ESO

Typically, the conventional ESO is designed with the bandwidth-parameterization method [25] that sets the characteristic polynomial as follows:

$$\Phi(s) = \begin{cases} \left(s^2 + 2\xi\omega_o s + \omega_o^2\right)^{k/2}, & k \text{ is even} \\ \left(s^2 + 2\xi\omega_o s + \omega_o^2\right)^{(k-1)/2}(s + \omega_o), & k \text{ is odd} \end{cases} \tag{12}$$

where k is the order of ESO, ω_o is defined as the bandwidth of ESO, and $\xi = 1$ is assumed in later discussion for convenience.

The observer gain $\boldsymbol{L}$ can be obtained with the *acker* function in MATLAB or by solving (12), and the latter gives an analytical solution. When $k = 2$, $\boldsymbol{L}$ is obtained as

$$\boldsymbol{L} = \begin{bmatrix}l_1\ l_2\end{bmatrix}^T = \begin{bmatrix}a_0 + 2\xi\omega_o\ \omega_o^2/b_0\end{bmatrix}^T. \tag{13}$$

The resultant response $S_d(s)$ for disturbance estimation is calculated as (14). The selection of ω_o is a tradeoff between dynamic performance and noise immunity. A large ω_o will speed up the estimation but amplify the measurement noise. Due to the limited ω_o, (14) only realizes accurate tracking for dc disturbance. It indicates the conventional ESO is insufficient for the estimation of harmonic disturbance

$$S_d^{\text{ESO}}(s) = \tilde{d}(s)/d(s) = \frac{s(s + 2\xi\omega_o)}{s^2 + 2\xi\omega_o s + \omega_o^2} = 1 - T_d^{\text{ESO}}(s). \tag{14}$$

B. Single Harmonic Disturbance

The study of EHSO is beginning with a single harmonic disturbance. In this case, the observer in (8) is fourth order with two additional states for the harmonic observation. The first attempt to design the EHSO is taking the suggestions in [25] again that all the observer poles are placed according to (12) with $k = 4$. However, it may not be a good solution. The corresponding $S_d(s)$ is calculated as (15). It has a zero at origin and two zeros at $\pm\mathrm{j}\omega_h$, indicating the observer has zero steady-state estimation error at dc and ω_h

$$S_d(s) = \frac{\tilde{d}(s)}{d(s)} = \frac{s\left(s^2 + \omega_h^2\right)(s + 4\xi\omega_o)}{\left(s^2 + 2\xi\omega_o s + \omega_o^2\right)^2} = 1 - T_d(s). \tag{15}$$

Although the poles alone determine the type of transient response, it is the combined pole-zero pattern that determines the transient performance. The zeros $\pm\mathrm{j}\omega_h$ are far away from the poles at $s = -\omega_o$, and they get farther as ω_h increases. Since

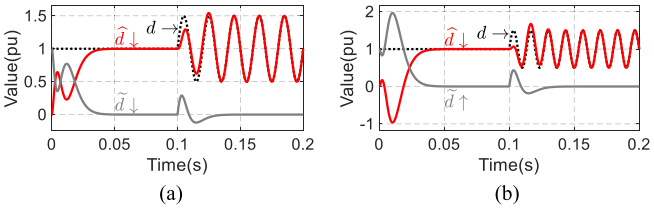

Fig. 2. Responses of the estimated disturbance and error when four identical observer poles are assigned with $\omega_o = 300$ rad/s and $\xi = 1$. (a) $\omega_h = 100\pi$ rad/s. (b) $\omega_h = 150\pi$ rad/s.

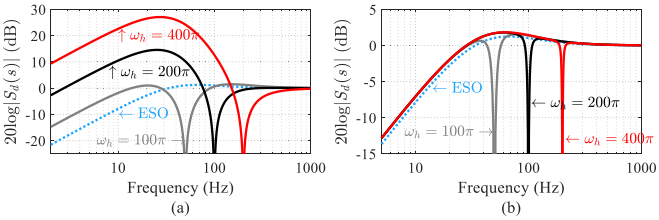

Fig. 3. Magnitude plot of $S_d(s)$. $\omega_o = 300$ rad/s and $\xi = 1$ are used. (a) EHSO with four identical poles. (b) EHSO with the proposed design (17) and $\rho = 30$ rad/s.

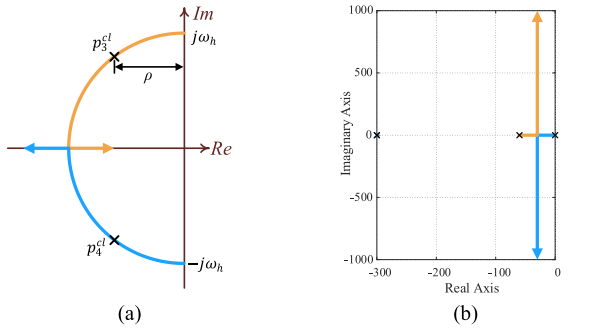

Fig. 4. Loci of the observer poles. (a) Two resonant poles with ρ varing. (b) ω_h varies from 0 to 1000 rad/s. $\omega_o = 300$ rad/s, $\xi = 1$.

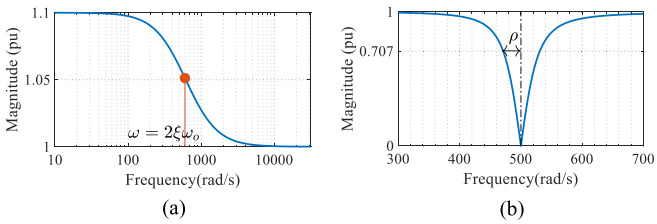

Fig. 5. Magnitude plot of the (a) second term and (b) third term in (18). $\omega_o = 300$ rad/s, $\xi = 1$ and $\rho = 30$ rad/s, $\omega_h = 500$ rad/s.

no near poles cancel their effect, the two zeros have a significant impact on the dynamic performance of disturbance estimation and the impact grows with ω_h. Fig. 2 shows the responses of disturbance estimation under various ω_h. The estimated disturbance $\hat{d}$ can accurately track the sinusoidal disturbance d in both Fig. 2(a) and (b); however, as for the disturbance unit step, the estimated value shows a remarkable fluctuation, and the fluctuation gets more seriously in Fig. 2(b) with a higher ω_h. Furthermore, undershoot arises in Fig. 2(b). In this case, the observer is even providing wrong information about the disturbance d.

The magnitude plot of $S_d(s)$ in Fig. 3(a) further verifies the results. $S_d(s)$ has a wide notch around ω_h; however, the low-frequency range is lifted as ω_h increases. These are coincident with Fig. 2 that the estimation error $\tilde{d}$ quickly converges to zero for the sinusoidal disturbance while the unit step response is bad. It will be shown in Section IV that $S_d(s)$ also represents the disturbance rejection capability of the closed-loop system. Hence, the effect of disturbance will be strengthened in the range of $|S_d(s)|$ beyond 0 dB. In addition, the high peak of $S_d(s)$ implies a rather poor robustness [29].

Such phenomenon can be interpreted by the water-bed effect introduced in Bode integral theorem [30]: if the sensitivity is pulled down in some frequency range then it had to pop up somewhere else. In this sense, the estimating for constant disturbance and for harmonic disturbance compete internally, and it is the wide notch around ω_h that causes the observed high sensitivity in Fig. 3(a). In other words, to reduce sensitivity peak in the low-frequency range, the bandwidth for the harmonic estimation should be limited.

Therefore, the assignment of the observer poles to the same locations may not be a good choice when the harmonic-observation functionality is added, especially for a large ω_h. The design criteria in [20] that assign observer poles to locations much faster than the harmonic frequencies would also lead to a similar problem.

In PMSM drives, the major harmonic disturbance, such as the cogging torque, is usually slow-varying (with respect to the magnitude and initial phase), thus there is also no need for very fast convergence for the harmonic disturbance. Since $S_d(s)$ always has the two zeros $\pm j\omega_h$, an alternative pole-placement strategy is that two poles are put near $\pm j\omega_h$ to counteract their influence, whereas the other two poles remain being characterized by $(s^2 + 2\xi\omega_o s + \omega_o^2)$. Based on this idea, the characteristic polynomial is suggested as

$$\Phi\ (s) = \left(s^2 + 2\xi\omega_o s + \omega_o^2\right)\ \left(s^2 + 2\rho s + \omega_h^2\right) \tag{16}$$

where the two poles involved in the harmonic disturbance estimation are selected by $(s^2 + 2\rho s + \omega_h^2)$, and $\rho \ll \omega_o$ provides the damping. Fig. 4(a) shows the locations of the two poles. Increasing ρ results in more damped observer poles, and thus faster convergence for the target harmonic estimation. Fig. 4(b) shows the loci of the two resonant poles with the harmonic frequency ω_h varying. When $\omega_h < \rho$, the two poles will locate at the real axis of the s-plane.

The observer gain is solved as (17) and the corresponding $S_d(s)$ is calculated as (18). Fig. 3(b) shows the magnitude plot of $S_d(s)$ of the proposed design, where ESO is also compared as a baseline. Equation (18) interprets the relationship in the frequency response of $S_d(s)$ between ESO and the proposed design. Compared to ESO, the second term in (18) lifts up the magnitude below the frequency $2\xi\omega_o$, and the dc gain is $(1+\rho/\xi\omega_o)$, as demonstrated in Fig. 5(a). The third term is a notch filter at ω_h whose notch width is approximately defined by ρ for a large ω_h, as demonstrated in Fig. 5(b); it also dominates the notch shape in $S_d(s)$. The frequency properties of the second and third terms also verify the water-bed effect of Bode integral

theorem. Nevertheless, the ESO and the proposed EHSO has a similar tendency at frequencies other than ω_h, as shown in Fig. 3(b). It shows the proposed EHSO can accurately track the harmonic disturbance meanwhile reserve most characteristic of ESO. In addition, since the notches in Fig. 3(b) are much narrower than those in Fig. 3(a), the sensitivity peak is reduced.

$$\boldsymbol{L}=\begin{bmatrix} l_1 \\ l_2 \\ l_3 \\ l_4 \end{bmatrix}=\begin{bmatrix} a_0+2\xi\omega_o+2\rho \\ \omega_o^2/b_0 \\ 4\xi\rho\omega_o/b_0 \\ 2\rho\left(\omega_o^2-\omega_h^2\right)/b_0 \end{bmatrix} \tag{17}$$

$$S_d(s)=\overbrace{\frac{s\left(s+2\xi\omega_o\right)}{s^2+2\xi\omega_o s+\omega_o^2}}^{S_d^{\mathrm{ESO}}(s)}\frac{s+2\xi\omega_o+2\rho}{s+2\xi\omega_o}\frac{s^2+\omega_h^2}{s^2+2\rho s+\omega_h^2}. \tag{18}$$

C. Multiple Harmonic Disturbance

Based on the previous analyses, the expected characteristic polynomial of the DOB with n harmonics can be defined as

$$\Phi(s)=\left(s^2+2\xi\omega_o s+\omega_o^2\right)\prod_{k=1}^{n}\left(s^2+2\rho_k s+\omega_{h_k}^2\right) \tag{19}$$

where ρ_k controls the level of selectivity for the harmonic state with frequency ω_{h_k}. Consequently, the sensitivity function is obtained as

$$S_d(s)=S_d^{ESO}(s)\frac{s+2\xi\omega_o+2\sum_{k=1}^{n}\rho_k}{s+2\xi\omega_o}\times\prod_{k=1}^{n}\frac{s^2+\omega_{h_k}^2}{s^2+2\rho_k s+\omega_{h_k}^2}. \tag{20}$$

The third term in (20) provides notches at the selected frequencies. The dc gain of the second term is $1+\sum_{k=1}^{n}\rho_k/\xi\omega_o$, indicating that all the gains of harmonic observation contribute to magnitude amplification of $S_d(s)$ at low frequencies. This is the cost to incorporate more harmonic states to the observer. Increasing ξ and ω_o can alleviate the magnitude amplification. On the other hand, ρ_k can be decreased accordingly as the number of observed harmonics increases.

To maintain a similar performance of EHSO to ESO in tracking low-frequency disturbance, the adjustment of ξ and ω_o can be performed as the following procedure. If there has been an ESO parameterized by $\bar{\omega}_o$ and $\bar{\xi}$, and the EHSO expects a similar frequency response in the low-frequency range, solving

$$\frac{S_d(s,\omega_o,\xi)}{S_d^{ESO}\left(s,\bar{\omega}_o,\bar{\xi}\right)}\Big|_{s=0}=1 \tag{21}$$

yields

$$\omega_o=\frac{\xi\bar{\omega}_o+\sqrt{\xi^2\bar{\omega}_o^2+4\bar{\xi}\bar{\omega}_o\sum_{k=1}^{n}\rho_k}}{2\bar{\xi}}\approx\frac{\xi}{\bar{\xi}}\bar{\omega}_o+\frac{1}{\xi}\sum_{k=1}^{n}\rho_k. \tag{22}$$

Equation (22) can be used to adjust ω_o and ξ, and approximation is valid for $\bar{\omega}_o\gg\sum_{k=1}^{n}\rho_k$. In this case, for $\xi=\bar{\xi}=1$, (22) shows $\sum_{k=1}^{n}\rho_k$ should be superposed in ω_o compared to the original ESO bandwidth $\bar{\omega}_o$. Fig. 6(a) shows the effect of adjusting ω_o and ξ based on (22), where the ESO and EHSO has

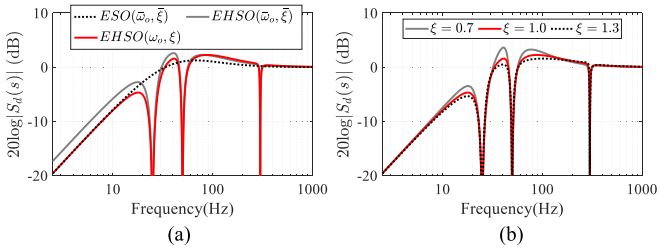

Fig. 6. Adjustment of ω_o and ξ according to (22). (a) Comparison between ESO and EHSO. $\xi=1$. (b) Various ξ. Other conditions are the same for (a) and (b) that $\bar{\omega}_o$= 300 rad/s, $\bar{\xi}$= 1, ρ_1=ρ_2 =ρ_3 = 30 rad/s.

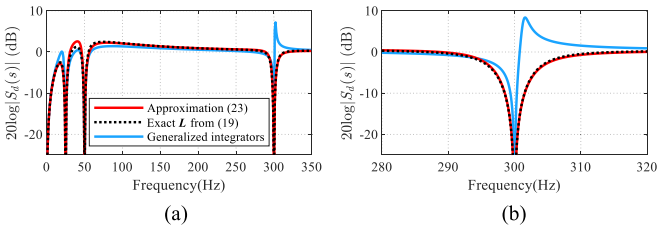

Fig. 7. (a) Comparision of $S_d(s)$ with different observer gain $\boldsymbol{L}$. (b) Zoomed view of (a).

consistent frequency response at the low-frequency range. Comparing traces of EHSO with $\bar{\omega}_o$ and ω_o (noting that $\xi=\bar{\xi}=1$), it also demonstrates the effect of increasing ω_o on reducing the sensitivity function. Fig. 6(b) shows the frequency response with various ξ and the resultant ω_o from (22). Increasing ξ can further reduce the sensitivity function peak. However, this is at the expense of utilizing a higher ω_o, which would amplify the measurement noise. Therefore, the compromise between the dynamic performance and noise immunity is still required.

However, the solution $\boldsymbol{L}$ of (19) is forbiddingly complex as n grows. The direct extension of (17) as below can be a feasible simplification of $\boldsymbol{L}$ for $\rho_k\ll\omega_o$, which can reduce the online computational load

$$\begin{cases} l_1=a_0+2\xi\omega_o+2\sum_{k=1}^{n}\rho_k \\ l_2=\omega_o^2/b_0 \\ l_{2k+1}\approx 4\xi\rho_k\omega_o/b_0,\ k=1,2,\ldots,n \\ l_{2k+2}\approx 2\rho_k\left(\omega_o^2-\omega_{hk}^2\right)/b_0 \end{cases}. \tag{23}$$

Fig. 7(a) shows an example of the frequency response of $S_d(s)$ with multiple harmonics, where the difference between using the simplified gain (23) and the exact $\boldsymbol{L}$ solved from (19) is negligible. Fig. 8(a) demonstrates the root loci of the observer poles when three harmonics are to be estimated. For convenience, $\rho_1=\rho_2=\rho_3=\rho$ is used (they can also be set independently). Due to the symmetry, only the second quadrant of s plane is shown. From the zoomed view in Fig. 8(a), three trajectories (highlighted by different colors) are in relation to the three estimated harmonics, and they are aside by the circles whose radiuses are $h_1\omega_m$, $h_2\omega_m$, and $h_3\omega_m$, respectively. For a small ρ, e.g., $\rho=10$, 20, or 30, the real parts of the corresponding poles are close to $-\rho$ as expected. As ρ further increases, the deviation become larger, since (23) is only an approximation after all. Nevertheless, Fig. 8(a) shows that the observer poles with (23) will locate near the expected positions for small ρ_k.

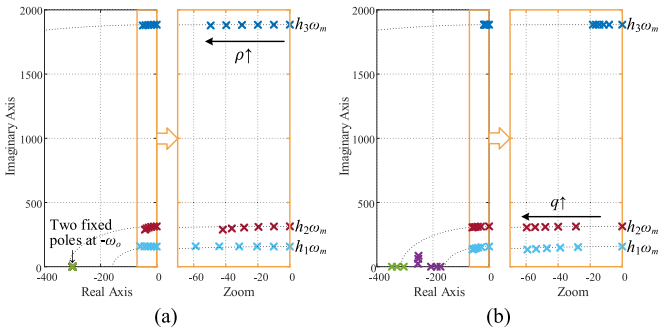

Fig. 8. Root loci of the observer poles. The harmonic orders are $h_1 = 1$, $h_2 = 2$, $h_3 = 12$, and the rotor speed is $\omega_m = 50\pi$ rad/s. (a) Proposed design with the gain in (23), $\rho_1 = \rho_2 = \rho_3 = \rho$ with ρ increased from 0 to 50 by step 10, and $\omega_o = 300$ rad/s. (b) LQR design with $N = 0.01^2$ and q increased from 0 to 5 by step 1.

The work in [19] incorporates parallel generalized integrators to the ESO for harmonic state observation, which is equivalent to setting $l_{2k+2} = 0$ and only regarding l_{2k+1} in (23) as the integral coefficients. The underutilization of the coefficient freedom can lead to inferior dynamic performance, as the anomalous peak of the cyan trace shown in Fig. 7(b), indicating a poor robustness. It also makes the observer sensitive to frequency deviation. As a result, Guo *et al.*'s work [19] has to use a rather large damping coefficient $\xi \geq 4$ to meet the requirement of phase margin, but the response for low-frequency disturbance will be slowed consequently.

D. Comparison With the LQR Design

Though the LQR design is claimed previously to be not feasible for EHSO in variable-speed PMSM drives due to computational complexity, it is still interesting to compare the proposed design with LQR design under fixed harmonic frequencies. Two parameters are utilized in the LQR approach, N for measurement noise and matrix $\boldsymbol{Q}$ for process noise (or model uncertainty). Now, the selecting of the observer gain becomes an optimization problem that minimizes the estimation error in the time domain from an H^2 sense, and the relationship N between and $\boldsymbol{Q}$ determines the observer bandwidth.

However, for the multifrequency design task in EHSO, the selection of the matrix $\boldsymbol{Q}$ still needs trial-and-error to balance the weight on the observer states that have different time scale. In this scenario, we are to explore the locations of poles related to the harmonic states, whereas other poles (involved to estimate speed and the dc disturbance) are not the major concerns. Therefore, an example of $\boldsymbol{Q}$ for three harmonics is evaluated and given below, where the weight coefficients for the harmonic states $\hat{w}_{h1}, \hat{w}_{h2}$, and $\hat{w}_{h3}$ are set equal

$$\boldsymbol{Q} = \text{diag}\left(15, 600^2, 10^5 q, 0, 10^5 q, 0, 10^5 q, 0\right). \tag{24}$$

Fig. 8(b) shows the observer poles for a sweep in q of (24). As q increases, the poles corresponding to the harmonic states move away from the imaginary axis, and they are also aside by the circles with the radius being $h_1\omega_m, h_2\omega_m$, and $h_3\omega_m$, respectively, which is similar with the proposed design. Such similarity indicates the round trajectory defined in Fig. 4(a) can

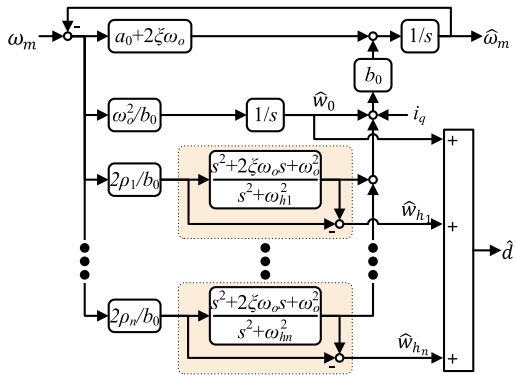

Fig. 9. Block diagram of the EHSO for estimation of multiple harmonics.

be considered as a quasi-optimal solution for the EHSO. Besides, though the same weight coefficients for the three harmonic states are used in Fig. 8(b), the distances of the harmonic poles to the imaginary axis are different, which indicates further adjustment in $\boldsymbol{Q}$ is required to control the level of selectivity for each harmonic disturbance. However, this can be easily realized by changing ρ_k in the proposed design.

E. Modular Structure and Discretization

Notably, the dynamics of the observer can be expressed as

$$\begin{aligned}\hat{\omega}_m &= \frac{1}{s}\left[\left(l_1 + b_0\frac{l_2}{s} + b_0\sum_{k=1}^{n}\frac{s l_{2k+1} + l_{2k+2}}{s^2+\omega_{hk}^2}\right)e + b_0 i_q\right] \\ &= \frac{1}{s}\left[\left(a_0 + 2\xi\omega_o + \frac{\omega_o^2}{s}\right)e + b_0 i_q\right] \\ &\quad + \frac{2}{s}\sum\nolimits_{k=1}^{n}\rho_k R\left(s,\omega_{h_k}\right)e \end{aligned} \tag{25}$$

where $e = \omega_m - \hat{\omega}_m$, and the dependence of signals on the Laplace operator s is omitted for brevity. $R(s,\omega_h)$ is given by

$$R\left(s,\omega_h\right) = \frac{s^2 + 2\xi\omega_o s + \omega_o^2}{s^2+\omega_h}$$

and the estimated harmonic state can be rewritten as

$$\hat{w}_{\alpha k} = \frac{s l_{2k+1} + l_{2k+2}}{s^2+\omega_{hk}^2}e = \frac{2}{b_0}\sum_{k=1}^{n}\rho_k\left(R\left(s,\omega_{h_k}\right) - 1\right)e. \tag{26}$$

The first term in (25) represents the dynamics of the second-order ESO. According to (25) and (26), the estimation for each harmonic state is involved with $R(s,\omega_{h_k})$, and it is worked as an add-on to the conventional ESO. Therefore, a modular structure of the proposed EHSO can be established in Fig. 9. It should be noted that the system is observable if $\omega_m \neq 0$. For a stable operation, the estimation for harmonic disturbance should be disabled around zero speed range, whereas the ESO part remains working.

The crucial consideration for the discretization of the resonant term is to preserve the frequency characteristic around the resonant frequency so that the observer can provide an accurate estimation of the target harmonics. Tustin with prewarping is utilized in this article for its simplicity and no need to calculate z-transformation. For a specific $R(s,\omega_h)$, the prewarp

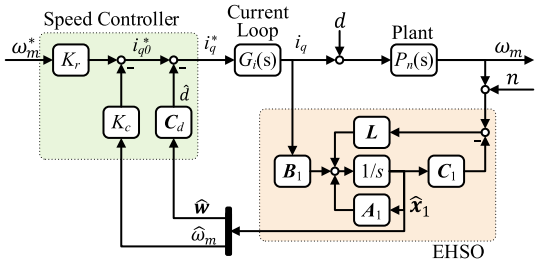

Fig. 10. Block diagram of the control system.

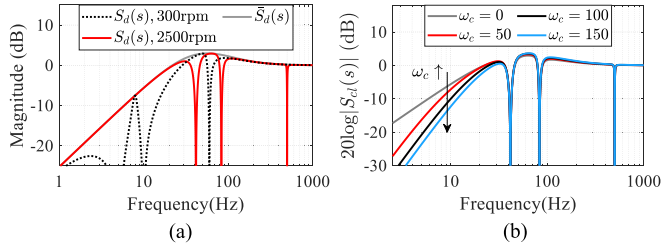

Fig. 11. (a) Comparision between $\bar{S}_d(s)$ and $S_d(s)$. (b) Comparision of $S_{cl}(s)$ with various ω_c at 2500 r/min. The harmonic orders are h_1=1, h_2=2, and h_3=12. ω_o=300 rad/s, ξ=1, ρ_1=ρ_2=ρ_3=30 rad/s, a_0=0. The observer gain in (23) is employed.

frequency is ω_h, and the discretization is realized by the substitution $s \to \frac{2}{\beta T_s} \cdot \frac{z-1}{z+1}$, where T_s is the sampling period and $\beta = 2\tan(\omega_h T_s/2)/(\omega_h T_s)$. This yields

$$R(s,\omega_h)|_{s=\frac{2}{\beta T_s},\frac{z-1}{z+1}} = g_d \frac{\alpha_2 z^2 + \alpha_1 z + \alpha_0}{z^2 - 2z\cos\omega_h T_s + 1} \tag{27}$$

where

$$g_d = \frac{2(1-\cos\omega_h T_s)}{\omega_h^2 \beta^2 T_s^2}, \alpha_0 = \tfrac{1}{4}\omega_o^2\beta^2 T_s^2 - \xi\omega_o\beta T_s + 1$$
$$\alpha_1 = \tfrac{1}{2}\omega_o^2\beta^2 T_s^2 - 2, \alpha_2 = \tfrac{1}{4}\omega_o^2\beta^2 T_s^2 + \xi\omega_o\beta T_s + 1.$$

Thereafter, the poles $z = e^{\pm j\omega_h T_s}$ of (27) guarantee the infinite gain at the resonant frequencies.

IV. Torque Ripple Elimination With EHSO

After the harmonic disturbance has been accurately estimated, it can be attenuated in a feedforward manner. Assuming a fast enough current loop at the frequencies of interests, i.e., $i_q \approx i_q^*$, the speed controller is formed as a two-degree-of-freedom structure given in (28), where ω_m^* is the speed reference, K_r and K_c are the controller parameters, and i_{q0}^* is the control effort without feedforwarding the estimated disturbance $\hat{d}$

$$i_q \approx i_q^* = \underbrace{K_r\omega_m^* - K_c\hat{\omega}_m}_{i_{q0}^*} - \hat{d}. \tag{28}$$

The block diagram of the control system is shown in Fig. 10. According to the bandwidth-parameterization method [25], $K_c = b_0^{-1}(\omega_c + a_0)$ is obtained with ω_c being the bandwidth for reference tracking, and $K_r = b_0^{-1}\omega_c$ is selected to remove steady-state error for a constant speed command. The transfer function for reference tracking is obtained as

$$G_r(s) = \frac{\omega_m(s)}{\omega_m^*(s)} = \frac{\omega_c}{s+\omega_c}. \tag{29}$$

A. Robustness Analysis

Considering the inner loop where only the estimated disturbance $\hat{d}$ is compensated, the rotor speed can be formulated as

$$\omega_m = P_n(s)(i_{q0}^* - \hat{d} + d) = P_n(s)i_{q0}^* + S_d(s)P_n(s)d \tag{30}$$

where $P_n(s) = b_0/(s-a_0)$ is the nominal plant model.

Equation (30) shows $S_d(s)$ is also the sensitivity function of the inner loop that determines disturbance rejection property. The internal model principle points out that the controller incorporating an internal model of the exogenous signals is insensitive to plant parameter variations. This is verified here, as $S_d(s) = 0$ is ensured for the frequencies defined by $\det(j\omega\boldsymbol{I} - \boldsymbol{A}_d) = 0$.

Sometimes it is not easy to illustrate the gain margin (GM) and phase margin (PM) of the multifrequency control system due to multiple crossover events. Here, the sensitivity peak of $S_d(s)$ denoted by M_s is introduced to indicate the relative stability. There is a close relationship between M_s and the stability margins. Especially, for a given M_s, the following GM and PM are guaranteed [29]:

$$\text{GM} \geq \frac{M_s}{M_s-1}, \text{PM} \geq 2\arcsin\frac{1}{2M_s} \geq \frac{1}{M_s}\,[\text{rad}]. \tag{31}$$

To evaluate the sensitivity peak for $S_d(s)$, we note that the third term in (20) is a series of notches whose magnitude does not exceed 1. Therefore, the first two terms of (20), given by (32), are to be studied as the envelope curve for $S_d(s)$

$$\bar{S}_d(s) = \frac{s\left(s + 2\xi\omega_o + 2\sum_{k=1}^{n}\rho_k\right)}{s^2 + 2\xi\omega_o s + \omega_o^2}. \tag{32}$$

Fig. 11(a) compares the magnitude plot of $\bar{S}_d(s)$ and $S_d(s)$, where the traces of $S_d(s)$ with various harmonic frequencies are covered by $\bar{S}_d(s)$. By solving $\mathrm{d}|\bar{S}_d(j\omega)|/\mathrm{d}\omega = 0$, the maximum value can be obtained. The analytical result is complicated, however, there is a much simpler solution for $\xi = 1$

$$M_s \leq \max_\omega \left|\bar{S}_d(j\omega)\right| = \frac{2\left(\omega_o + \sum_{k=1}^{n}\rho_k\right)}{\omega_o\sqrt{\left(3\omega_o + 2\sum_{k=1}^{n}\rho_k\right)\left(\omega_o + 2\sum_{k=1}^{n}\rho_k\right)}}. \tag{33}$$

If $\sum_{k=1}^{n}\rho_k \leq 0.3\,\omega_o$, $M_s \leq 1.4$ can be obtained based on (33). Consequently, GM $\geq$ 10 dB and PM $\geq 41°$ are guaranteed for the inner loop according to (31).

For the closed-loop system, the sensitivity function is calculated by combining (2), (8), and (28) as

$$S_{cl}(s) = \frac{y(s)}{n(s)} = [1,\boldsymbol{0}]\left(s\boldsymbol{I} - \begin{bmatrix} a_0 & -b_0\boldsymbol{K} \\ \boldsymbol{L}\boldsymbol{C} & \boldsymbol{A}_1 - \boldsymbol{B}_1\boldsymbol{K} - \boldsymbol{L}\boldsymbol{C}_1 \end{bmatrix}\right)^{-1}\begin{bmatrix} 0 \\ \boldsymbol{L} \end{bmatrix} + 1 \tag{34}$$

where $\boldsymbol{K} = [K_c, \boldsymbol{C}_{1d}]$.

According to Fig. 10, $S_d(s)$ is a special case of $S_{cl}(s)$ when $K_c = b_0^{-1}(\omega_c - a_0) = 0$. The comparision of $S_{cl}(s)$ with various ω_c is shown in Fig. 11(b). They differ mainly in the low-frequency range depending on ω_c, whereas are quite close in the middle- and high-frequency range. Therefore, for $\omega_c < \omega_o$, the stability margin estimated by the sensitivity peak

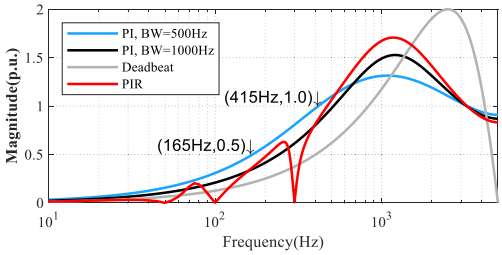

Fig. 12. Frequency responses of $|1 - G_i(s)|$ for various current controllers. The PI controller refers to the current controller proposed in [31]. The deadbeat control is modeled as a two-step delay (at 10-kHz sampling frequency). The resonant frequencies of PIR controller are 50, 100, and 300 Hz.

of $S_d(s)$, according to (31), can also be an approximation for the closed-loop system.

B. Impact of the Current Loop

Previous analyses assume ideal current control, i.e., $i_q = i_q^*$. However, this assumption holds only within a limited frequency range. Denotes the transfer function of the current loop as $G_i(s) = i_q(s)/i_q^*(s)$, and rotor speed can be expressed as

$$\omega_m = P_n(s)\, G_i(s)\, i_{q0}^* + [1 - G_i(s) + S_d(s)\, G_i(s)]\, P_n(s)\, d. \tag{35}$$

Although the EHSO has achieved zero steady-state estimation error at harmonic frequencies of interest, (35) shows that the disturbance cannot be fully compensated by feedforwarding $\hat{d}$ if perfect current control $G_i(s) = 1$ is not realized. The tracking error of the current loop described by $1 - G_i(s)$ also determines the effectiveness of disturbance cancellation. Fig. 12 shows the frequency responses of $|1 - G_i(s)|$ for various current controllers. Taking the PI controller with 500-Hz bandwidth (BW) for example, $|1 - G_i(s)|$ crosses the magnitude 0.5 and 1.0 at 165 and 415 Hz, respectively. In this case, even if the harmonic disturbance has been accurately estimated, the components within 165 Hz can be attenuated down to 50% by the control effort, but the components over 415 Hz will be amplified.

To realize full elimination of the speed-loop disturbance at specific frequencies, the current control should also provide zero steady-state error at the same frequencies. The resonant controller providing infinite gain at the target resonant frequency can be added to the current loop. Another benefit of utilizing the resonant control is that the current harmonics can be also suppressed. In this article, the PIR controller proposed in [32] will be used for the current loop. The red line in Fig. 12 shows the reference-tracking error of the PIR controller with three resonant frequencies. It is zero at these resonant frequencies. Thus, according to (35), the harmonic disturbances of interest are theoretically rejected.

V. Experiments

The experimental setup is shown in Fig. 13. The experiments are conducted on a three-phase PMSM connected to a voltage source inverter with the parameters being pole-pairs $P_r = 2$, phase resistance $R_s = 0.29\Omega$, inductance $L_s = 0.5$mH, and dc-bus voltage $u_{dc} = 30$V. The switching frequency is

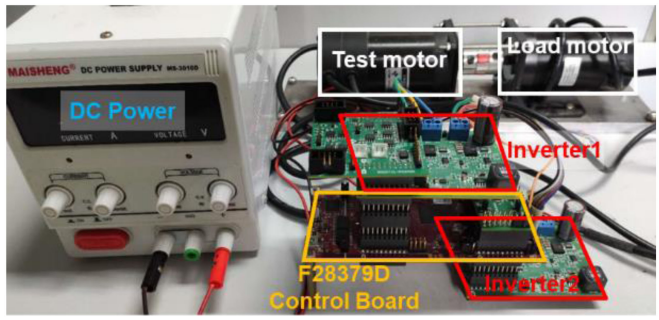

Fig. 13. Experimental setup.

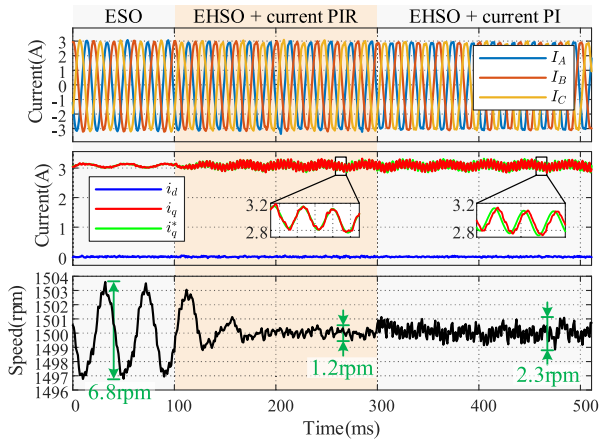

Fig. 14. Experimental results when the EHSO and current PIR controller.

$f_{sw} = 10$ kHz and single-sampling-single-updating scheme is applied. A quadrature encoder with 4096 counts/rev resolution is used for position and speed measurement. Another PMSM is mechanically coupled with the tested motor as a load. A control board equipped with a 200-MHz microcontroller is used for the control of both motors.

In the following experimental results, three harmonic disturbances with the frequency being the 1st, 2nd, and 12th of the mechanical frequency, respectively, are of interest for evaluating the performance of the proposed method. If no other specifications, the default control parameters are: $\omega_o = 300$, $\omega_c = 50$, $a \approx a_0 = 0$, $b \approx b_0 = 879.6$, $\rho_1 = \rho_2 = \rho_3 = 30$, current control gain $K_i = 0.3$ (all parameters are in SI unit).

A. Steady-State Performance

Fig. 14 shows the waveforms of three-phase current, *dq*-axes current, *q*-axis reference, and rotor speed under various control strategies. The load torque is applied to make i_q being about 3 A. The motor is initially operated under the conventional ESO with PI current controller, and the peak-to-peak of the measured speed is up to 6.8 r/min at this stage. At 100 ms, the system switches to the proposed EHSO with PIR current controller. It takes about 70 ms to settle down and the peak-to-peak speed is 1.2 r/min, which is a significant reduction from the previous value. It also demonstrates the rapidity of the proposal in estimating and suppressing harmonic disturbance. After 300 ms, the resonant control of the current loop is disabled, thus only

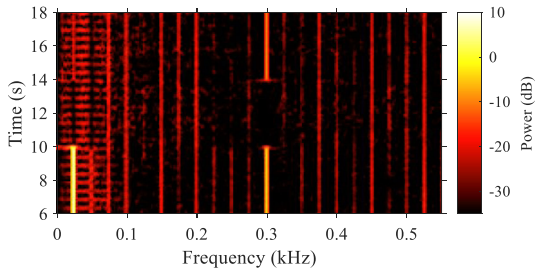

Fig. 15. Spectrogram of measure speed at 1500 r/min. The motor is operated under ESO and PI current controller before 10 s, and then switched to the proposed EHSO with PIR current controller. At about 14 s, the resonant control of the current loop is disabled.

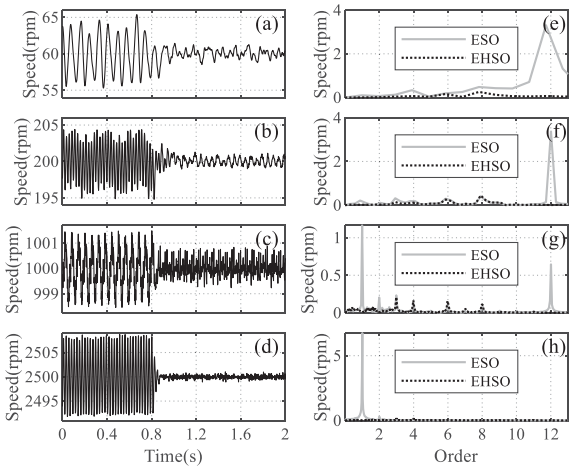

Fig. 16. Compensation results of (a)–(d) speed responses and (e)–(h) harmonic analyses at speed 60, 200, 1000, and 2500 r/min, respectively. ESO is enabled before 0.8 s and EHSO is enabled at 0.8 s.

a current PI controller is activated. Phase lag arises between i_q and its reference i_q^*. As analyzed in Section V, the current PI controller is incapable to compensate for the high-frequency speed disturbance. Therefore, the speed ripple is a bit increased and the peak-to-peak value reaches 2.3 r/min.

The spectrogram of rotor speed at 1500 r/min is shown in Fig. 15, which is obtained by applying short-time Fourier transform to long-term speed data. The horizontal slice indicates the frequency information at the corresponding time. If a component with a specified frequency persistently exists, a vertical line will appear. Two bright lines at 25 and 300 Hz and a light line at 50 Hz can be observed before 10 s when ESO is implemented, and they are blackened when the proposed EHSO with PIR current controller is enabled during 10–14 s. After the resonant current control is disabled at 14 s, the lines at 25 and 300 Hz emerge but are darker than those before 10 s. This further verifies the necessity of employing resonant current controllers for zero-steady-state error at target harmonic frequencies.

Other compensation results at various speeds are shown in Fig. 16, and the harmonic analyses of speed and q-axis are also provided. It is found the 12th speed harmonics with respect to the mechanical frequency (or 6th order to the fundamental frequency) are dominant at the low-speed range, whereas the 1st speed harmonic is the most significant at higher speed range.

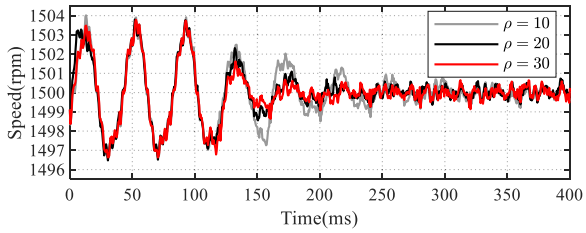

Fig. 17. Speed responses with various ρ. EHSO is enabled at 100 ms.

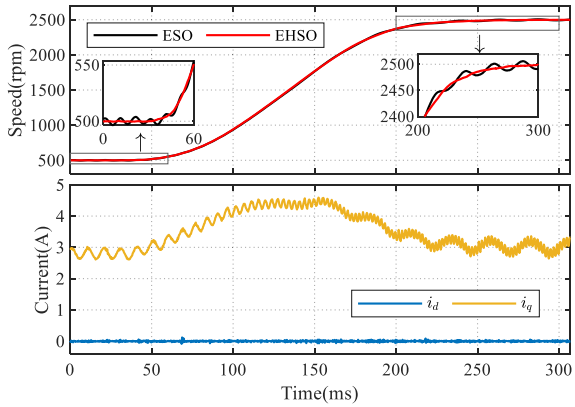

Fig. 18. Speed transition from 500 r/min to 2500 with the proposal.

This is because the rotational inertia has a stronger filtering effect for high-frequency speed harmonics and rotor eccentricity may be severer at higher speeds. Nevertheless, the speed ripples in all these occasions are reduced after the proposed EHSO is enabled.

Fig. 17 demonstrates the effect of the parameter ρ. It takes about 200 ms for $\rho = 10$ to settle down and less time for $\rho = 20$ and $\rho = 30$. A higher ρ resulted in faster disturbance estimation and attenuation. Thus, the convergence speed of the proposed EHSO can be easily tuned by ρ.

B. Dynamic Control Performance

Fig. 18 shows the experimental results with EHSO when the rotor speed ramps from 500 to 2500 r/min. It tests the performance of EHSO under a fast-varying speed where the maximum acceleration speed is up to 16 000 r/min/s. The speed trace of ESO under the same condition is added as the baseline. From the zoomed view of the speed signals at the start and end of the acceleration, the speed fluctuations with EHSO remain at a relatively low level. This verifies the stability as well as the harmonic disturbance rejection capability of the proposed EHSO under varying speeds.

The disturbance rejection performance is evaluated in Fig. 19, where the proposed EHSO is compared with the conventional ESO. Based on (22), the bandwidth ω_o for ESO is set 300 rad/s and for EHSO is set 390 rad/s for comparison. The load torque changes at around 50 ms. According to the i_q responses, both the ESO and EHSO has similar speed to respond to the disturbance. In the speed responses, although EHSO shows a different shape, they have a similar convergence speed and settling time. This demonstrates that the EHSO can realize comparable dynamic performance with ESO.

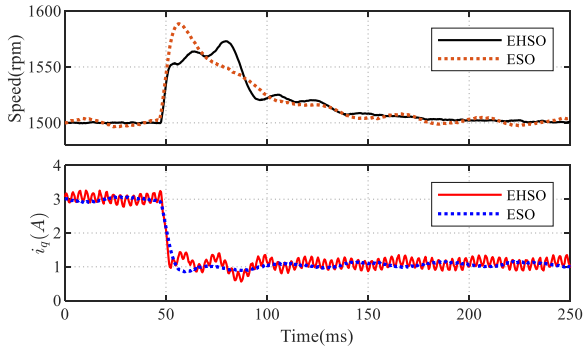

Fig. 19. Experimental results of speed and i_q for disturbance rejection.

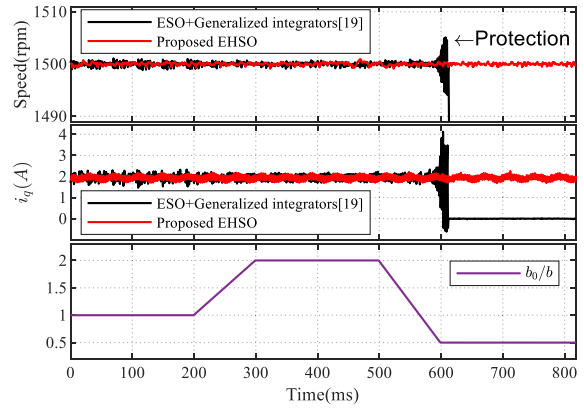

Fig. 20. Experimental test of various b_0.

Finally, the robustness of the proposed method is tested, as shown in Fig. 20. The most critical parameter relevant to the mechanical system is b_0, which is dependent on the total rotor inertia and the PM flux. In this test, b_0 profile is given as the third subgraph in Fig. 20. The speed control loop is stable during the test and no significant ripples arise, indicating the robustness of the proposed method in suppressing the harmonic disturbance. In addition, the ESO plus multiple generalized integrators [19] is also compared. When b_0/b is below about 0.75, the system loses stability and soon triggers the overcurrent protection. This verifies that the high sensitivity peak in Fig. 7 is corresponding to poor robustness, whereas the proposal has better relative stability.

VI. Conclusion

This article proposes an EHSO for the reduction of harmonic torque disturbance in PMSM drive. The internal model of the torque disturbance is embedded into the EHSO for zero-steady-state estimation error. To improve the robustness of the control system when the functionality of harmonic state estimation is added, the observer gain is optimally designed with a reduced closed-loop-system sensitivity function peak. The developed EHSO features a modular structure and uses one parameter for each harmonic state to adjust its estimation and attenuation speed. The requirement of the current loop for the harmonic disturbance rejection is analyzed and verified by the experiments. Future works will be concentrated on reducing the complexity of the whole speed and current control when the number of selected harmonics increases.

References

[1] X. Zhu, W. Hua, Z. Wu, W. Huang, H. Zhang, and M. Cheng, "Analytical approach for cogging torque reduction in flux-switching permanent magnet machines based on magnetomotive force-permeance model," *IEEE Trans. Ind. Electron.*, vol. 65, no. 3, pp. 1965–1979, Mar. 2018.

[2] J. Ou, Y. Liu, R. Qu, and M. Doppelbauer, "Experimental and theoretical research on cogging torque of PM synchronous motors considering manufacturing tolerances," *IEEE Trans. Ind. Electron.*, vol. 65, no. 5, pp. 3772–3783, May 2018.

[3] W. Deng and S. Zuo, "Analysis of the sideband electromagnetic noise in permanent magnet synchronous motors generated by rotor position error," *IEEE Trans. Ind. Electron.*, vol. 69, no. 5, pp. 4460–4471, May 2022.

[4] D. Wang, X. Wang, and S.-Y. Jung, "Cogging torque minimization and torque ripple suppression in surface-mounted permanent magnet synchronous machines using different magnet widths," *IEEE Trans. Magn.*, vol. 49, no. 5, pp. 2295–2298, May 2013.

[5] P. Wang, W. Hua, and G. Zhang, "Torque ripple suppression of flux-switching permanent magnet machine based on general air-gap field modulation theory," *IEEE Trans. Ind. Electron.*, early access, Dec. 29, 2021, doi: 10.1109/TIE.2021.3137617.

[6] D. M. Park and K. H. Kim, "Parameter-independent online compensation scheme for dead time and inverter nonlinearity in IPMSM drive through waveform analysis," *IEEE Trans. Ind. Electron.*, vol. 61, no. 2, pp. 701–707, Feb. 2014.

[7] M. Hu, W. Hua, Z. Wu, N. Dai, H. Xiao, and W. Wang, "Compensation of current measurement offset error for permanent magnet synchronous machines," *IEEE Trans. Power Electron.*, vol. 35, no. 10, pp. 11119–11128, Oct. 2020.

[8] Y. A. R. I. Mohamed and E. F. El-Saadany, "A current control scheme with an adaptive internal model for torque ripple minimization and robust current regulation in PMSM drive systems," *IEEE Trans. Energy Convers.*, vol. 23, no. 1, pp. 92–100, Mar. 2008.

[9] F. Bu *et al.*, "Speed ripple reduction of direct-drive PMSM servo system at low-speed operation using virtual cogging torque control method," *IEEE Trans. Ind. Electron.*, vol. 68, no. 1, pp. 160–174, Jan. 2021.

[10] G. Feng, C. Lai, X. Tan, B. Wang, and N. Kar, "Optimal current modeling and identification for fast and efficient torque ripple minimization of PMSM using theoretical and experimental models," *IEEE Trans. Ind. Electron.*, vol. 68, no. 12, pp. 11806–11816, Dec. 2021.

[11] Z. Wu, Z. Yang, K. Ding, and G. He, "Order-domain-based harmonic injection method for multiple speed harmonics suppression of PMSM," *IEEE Trans. Power Electron.*, vol. 36, no. 4, pp. 4478–4487, Apr. 2021.

[12] G. Feng, C. Lai, J. Tian, and N. C. Kar, "Multiple reference frame based torque ripple minimization for PMSM drive under both steady-state and transient conditions," *IEEE Trans. Power Electron.*, vol. 34, no. 7, pp. 6685–6696, Jul. 2019.

[13] J. Liu, H. Li, and Y. Deng, "Torque ripple minimization of PMSM based on robust ILC via adaptive sliding mode control," *IEEE Trans. Power Electron.*, vol. 33, no. 4, pp. 3655–3671, Apr. 2018.

[14] X. Huo, M. Wang, K.-Z. Liu, and X. Tong, "Attenuation of position-dependent periodic disturbance for rotary machines by improved spatial repetitive control with frequency alignment," *IEEE/ASME Trans. Mechatronics*, vol. 25, no. 1, pp. 339–348, Feb. 2020.

[15] M. Tang, A. Gaeta, A. Formentini, and P. Zanchetta, "A fractional delay variable frequency repetitive control for torque ripple reduction in PMSMs," *IEEE Trans. Ind. Appl.*, vol. 53, no. 6, pp. 5553–5562, Nov. 2017.

[16] M. Tang, A. Formentini, S. A. Odhano, and P. Zanchetta, "Torque ripple reduction of PMSMs using a novel angle-based repetitive observer," *IEEE Trans. Ind. Electron.*, vol. 67, no. 4, pp. 2689–2699, Apr. 2020.

[17] C. Xia, B. Ji, and Y. Yan, "Smooth speed control for low-speed high-torque permanent-magnet synchronous motor using proportional-integral-resonant controller," *IEEE Trans. Ind. Electron.*, vol. 62, no. 4, pp. 2123–2134, Apr. 2015.

[18] A. A. Godbole, J. P. Kolhe, and S. E. Talole, "Performance analysis of generalized extended state observer in tackling sinusoidal disturbances," *IEEE Trans. Control Syst. Technol.*, vol. 21, no. 6, pp. 2212–2223, Nov. 2013.

[19] B. Guo, S. Bacha, M. Alamir, A. Hably, and C. Boudinet, "Generalized integrator-extended state observer with applications to grid-connected converters in the presence of disturbances," *IEEE Trans. Control Syst. Technol.*, vol. 29, no. 2, pp. 744–755, Mar. 2021.

[20] M. Ruderman, A. Ruderman, and T. Bertram, "Observer-based compensation of additive periodic torque disturbances in permanent magnet motors," *IEEE Trans. Ind. Inform.*, vol. 9, no. 2, pp. 1130–1138, May 2013.
[21] Y. Yan, J. Yang, Z. Sun, C. Zhang, S. Li, and H. Yu, "Robust speed regulation for PMSM servo system with multiple sources of disturbances via an augmented disturbance observer," *IEEE/ASME Trans. Mechatron.*, vol. 23, no. 2, pp. 769–780, Apr. 2018.
[22] D. Pérez-Estévez, J. Doval-Gandoy, A. G. Yepes, and Ó. López, "Positive- and negative-sequence current controller with direct discrete-time pole placement for grid-tied converters with LCL filter," *IEEE Trans. Power Electron.*, vol. 32, no. 9, pp. 7207–7221, Sep. 2017.
[23] D. Pérez-Estévez, J. Doval-Gandoy, A. G. Yepes, Ó. López, and F. Baneira, "Generalized multifrequency current controller for grid-connected converters with LCL filter," *IEEE Trans. Ind. Appl.*, vol. 54, no. 5, pp. 4537–4553, Sep. 2018.
[24] C. Xia, N. Liu, Z. Zhou, Y. Yan, and T. Shi, "Steady-state performance improvement for LQR-based PMSM drives," *IEEE Trans. Power Electron.*, vol. 33, no. 12, pp. 10622–10632, Dec. 2018.
[25] Z. Q. Gao, "Scaling and bandwidth-parameterization based controller tuning," in *Proc. Amer. Control Conf.*, 2003, vol. 1–6, pp. 4989–4996.
[26] D. Pérez-Estévez, J. Doval-Gandoy, A. G. Yepes, Ó. López, and F. Baneira, "Enhanced resonant current controller for grid-connected converters with LCL filter," *IEEE Trans. Power Electron.*, vol. 33, no. 5, pp. 3765–3778, May 2018.
[27] G. Herbst, "Practical active disturbance rejection control: Bumpless transfer, rate limitation, and incremental algorithm," *IEEE Trans. Ind. Electron.*, vol. 63, no. 3, pp. 1754–1762, Mar. 2016.
[28] G. F. Franklin, J. D. Powell, and A. Emami-Naeini, *Feedback Control of Dynamic Systems*, 7th ed. Upper Saddle River, NJ, USA: Pearson Higher Education, 2014.
[29] S. Skogestad and I. Postlethwaite, *Multivariable Feedback Control: Analysis and Design*, 2nd ed. Hoboken, NJ, USA: Wiley, 2005.
[30] B.-F. Wu and E. A. Jonckheere, "A simplified approach to Bode's theorem for continuous-time and discrete-time systems," *IEEE Trans. Autom. Control*, vol. 37, no. 11, pp. 1797–1802, Nov. 1992.
[31] H. Kim, M. W. Degner, J. M. Guerrero, F. Briz, and R. D. Lorenz, "Discrete-time current regulator design for AC machine drives," *IEEE Trans. Ind. Appl.*, vol. 46, no. 4, pp. 1425–1435, Jul. 2010.
[32] M. Hu, W. Hua, G. Ma, S. Xu, and W. Zeng, "Improved current dynamics of proportional-integral-resonant controller for a dual three-phase FSPM machine," *IEEE Trans. Ind. Electron.*, vol. 68, no. 12, pp. 11719–11730, Dec. 2021.

Mingjin Hu (Student Member, IEEE) was born in Jiangxi, China, in 1994. He received the B.Sc. degree in electrical engineering in 2016 from the School of Electrical Engineering, Southeast University, Nanjing, China, where he is currently working toward the Ph.D. degree in electrical engineering.

His current research interests include the modeling and advanced control of electrical drives.

Wei Hua (Senior Member, IEEE) received the B.Sc. and Ph.D. degrees in electrical engineering from Southeast University, Nanjing, China, in 2001 and 2007, respectively.

From 2004 to 2005, he was with the Department of Electronics and Electrical Engineering, The University of Sheffield, Sheffield, U.K., as a Joint-Supervised Ph.D. Student.

Since 2007, he has been with Southeast University, where he is currently a Chief Professor of Southeast University and a Distinguished Professor of Jiangsu Province. In 2010, he has also worked with Yancheng Institute of New Energy Vehicles, Southeast University. He has coauthored more than 180 technical papers. He holds 70 patents in his areas of interest. His teaching and research interests include design, analysis, and control of electrical machines, especially for PM brushless machines and switching reluctance machines, etc.

Zuo Wang (Member, IEEE) was born in Xuzhou, China, in 1991. He received the B.Eng. degree in automation from Hohai University, Nanjing, China, in 2013, and the Ph.D. degree in control science and engineering from Southeast University, Nanjing, China, in 2020.

Since 2020, he has been with the School of Automation, Southeast University. From 2017 to 2018, he was a visiting Ph.D. student with the College of Engineering, University of Glasgow, Glasgow, U.K. His research interests include advanced control theory and its application to power electronics and ac motor control systems.

Shihua Li (Fellow, IEEE) received the B.E., M.E., and Ph.D. degrees in automatic control from Southeast University, Nanjing, China, in 1995, 1998, and 2001, respectively.

Since 2001, he has been with the School of Automation, Southeast University, where he is currently a Professor and the Director of Mechatronic Systems Control Laboratory. His main research interests include modeling, analysis, and nonlinear control theory with applications to mechatronic systems, including manipulator, robot, alternating current motor, power electronic systems, and others.

Peixin Wang (Student Member, IEEE) was born in Henan, China, in 1992. He received the B.S. and M.S. degrees in electrical engineering from Henan Polytechnic University, Jiaozuo, China, in 2016 and 2018, respectively. He is currently working toward the Ph.D. degree in electrical engineering with the School of Electrical Engineering, Southeast University, Nanjing, China.

His current research interests include design and analysis of permanent magnet and two-degree-of-freedom machines.

Yuchen Wang was born in Shanxi, China, in 1994. He received the B.Sc. degree in electrical engineering in 2017 from the School of Electrical Engineering, Southeast University, Nanjing, China. He is currently working toward the Ph.D. degree in electrical engineering with the School of Electrical Engineering, Southeast University.

His current research interests include the analysis and design of embedded magnetic encoder.